Short communication

Electrochemical performance studies of Li-rich cathode materials with different primary particle sizes

Jianhong Liu [a,b], Hongyu Chen [b], Jiaona Xie [b], Zhaoqin Sun [b], Ningning Wu [b], Borong Wu [a,*]

[a] School of Chemical Engineering and Environment, Beijing Institute of Technology, Beijing 100081, China
[b] CITIC Guoan Mengguli Power Science and Technology Co. Ltd, Beijing 102200, China

HIGHLIGHTS

- The spherical Li-rich materials with different primary particle sizes were synthesized.
- The materials with different primary particle sizes have different lattice strain.
- The relationship between the primary particle size and kinetics was discussed.
- The material with 200 nm primary particle shows the best electrochemical properties.

ARTICLE INFO

ABSTRACT

The spherical Li-rich materials $0.3Li_2MnO_3 \cdot 0.7LiNi_{0.5}Mn_{0.5}O_2$ are synthesized by a standard co-precipitation method followed by solid state sintering. The primary particle size and morphologies of the $0.3Li_2MnO_3 \cdot 0.7LiNi_{0.5}Mn_{0.5}O_2$ materials can be readily controlled by altering the heat-treatment temperature. With different primary size, the materials show different rate discharge capabilities. However, due to similar chemical composition, they show similar discharge capacity at high temperature and low current density. Subsequent galvanostatic intermittent titration tests indicate that the larger the particle size, the larger the chemical diffusion coefficient of the Li^+. The relationship between the primary particle size and electrochemical kinetics is discussed. Of all the samples in this study, the material with a primary particle size of 200 nm, obtained at 900 °C, exhibits the best integrated electrochemical performance.

1. Introduction

Li-ion batteries are used extensively in electric vehicles. The search for battery materials with higher energy density, longer cycle life and higher thermal stability continues. Many studies have been carried out to find alternative compositions that provide reversible capacity while maintaining structural stability. Recently discovered Li-rich materials in the form of layer−layer integrated $xLi_2MnO_3 \cdot (1 − x)LiMO_2$ (M = Ni, Mn, Co) are likely candidates to achieve a capacity objective of more than 200 mAh g^{-1}. However, such integrated compounds still suffer from poor rate capability, due to low electrochemical activity of the Li_2MnO_3 component [1–4]. At the end of the first discharge process, a fraction of the Li_2MnO_3 component is likely to be transformed from a layered structure to a spinel-like region. This phase transformation can reduce the rate of free migration of Li ions [5], even though sometimes increasing the temperature can eliminate this effect. On the other hand, the Li_2MnO_3 component is usually an insulating oxide and can cause high resistance during the electrochemical reaction [6]. These problems currently limit the use of Li-rich materials in real plug-in hybrid electric vehicles (PHEV) or hybrid electric vehicles (HEV).

There are many studies that have tried to enhance the ion and electron transport kinetics of the Li-rich materials, including cation doping [7–9], changing the Li_2MnO_3:$LiMO_2$ ratio [10] and coating the particle surface [3,4,11–14]. Usually, the Li^+ migration time t, Li^+ diffusion length L in the solid phase and Li^+ diffusion coefficient D_{Li^+}, can be described by the equation $t \approx L^2/D_{Li^+}$ [15,16]. It has been reported that it is more effective to improve the rate performance by shortening the Li ion migration length [17,18]. This has led to investigations into the use of nano-modification technology for cathode materials for Li-ion batteries in order to improve the rate performance [19–21]. Compared with the secondary particle size, the primary particle size has a greater influence on

* Corresponding author. Tel./fax: +86 010 89702984.
  E-mail addresses: ljh2962@aliyun.com, borongwu@gmail.com (B. Wu).

electrochemical and physical properties, such as electrolyte wetting, surface contact resistance and rate performance. However, a new problem must be faced for nano-scale particles, which is that the large specific surface area can cause more side-reactions during the charge−discharge process [22]. It is therefore essential to find a balance between the kinetic performance and the cyclic stability. This may be a feasible material design giving spherical shape particles with appropriate primary particle and secondary particle sizes.

In this paper, we describe the successful synthesis of a series of Li-rich layered cathode materials with the formula $0.3Li_2MnO_3 \cdot 0.7LiNi_{0.5}Mn_{0.5}O_2$. This can also be written as $Li_{1.130}Ni_{0.304}Mn_{0.565}O_2$ using the standard layered ($LiMO_2$) notation equivalent formula [6,23]. All the materials have spherical particles and a similar size distribution for the secondary particles, but with different nano-scale primary particle sizes. The relationship between the primary particle size and the electrochemical performance has been investigated using studies of lattice structure, particle morphologies, rate performance, and galvanostatic intermittent titration tests (GITT). Based on our experimental data, the material with 200 nm primary particle size exhibited the best integrated electrochemical performance.

2. Experimental

2.1. Synthesis of $0.3Li_2MnO_3 \cdot 0.7LiNi_{0.5}Mn_{0.5}O_2$ powders

A series of solid solution oxide materials with the formula $0.3Li_2MnO_3 \cdot 0.7LiNi_{0.5}Mn_{0.5}O_2$ were synthesized via a typical co-precipitation method. The synthesis process is as follows: an aqueous mixed solution of $NiSO_4$ and $MnSO_4$ with a concentration of 2.0 mol L^{-1} (Ni:Mn = 0.35:0.65, molar ratio) was pumped into a continuously stirred reactor (feeding rate: 6 mL min^{-1}). At the same time, a precipitating agent consisting of 4.0 mol L^{-1} NaOH solution and a prescribed amount of ammonium hydroxide solution (NH_4OH, 1.17 mol L^{-1}) as chelating agent were also separately fed into the reactor (feeding rate: 6 mL min^{-1}). A pH value of around 10.5 was maintained during the entire precipitation reaction. The temperature (55 °C) and stirring speed (1000 rpm min^{-1}) in the reactor were carefully controlled. After the co-precipitation was complete, the stirring was continued overnight. The precipitate was filtered off and washed with deionized water three times to eliminate residual sodium and sulfuric species. An ethanol exchange operation was carried out before being dried inside a vacuum oven (80 °C) for 8 h. Finally, the precursor was mixed with Li_2CO_3 (AR) at the chosen elemental ratio to give $0.3Li_2MnO_3 \cdot 0.7LiNi_{0.5}Mn_{0.5}O_2$. This was calcined at 800 °C, 900 °C and 1000 °C for 10 h in air, and the samples were named LM-8, LM-9 and LM-10, respectively.

2.2. Characterization and electrochemical test of powders

The particle morphologies of samples were characterized by field scanning electron microscopy (FSEM) on a Hitachi S-4800 instrument (Hitachi, Japan). X-ray diffraction (XRD) patterns of samples were collected on a Bruker D8 ADVANCE Powder Diffractometer with Cu Kα radiation ($\lambda = 1.5406$ Å) between 10 and 90° (40 kV, 40 mA, step size = 0.02° and count time of 0.2 s/step) to identify the crystalline phase of the materials. Lattice parameter determinations and lattice strain analyses were performed using the Bruker Topas 4.2 software. The specific surface areas of the powders were measured on a Gemini 2360 instrument (Micromeritics, USA). Particle size distributions of the powders were identified by a laser particle size analyzer (Beckman LS32, USA). The actual chemical compositions of the cathode materials were analyzed by inductively coupled plasma mass spectrometry (ICP-MS, ElanDRCII, Perkin Elmer, USA) measurement.

The electrochemical performances of $0.3Li_2MnO_3 \cdot 0.7LiNi_{0.5}Mn_{0.5}O_2$ were evaluated using CR-2032 type coin cells. Electrodes were made by casting a slurry of 90% weight active material oxide, 5% conductive reagent (Timcal, super-P), and 5% PVDF binder (Kynar, 761A) in N-methyl-2-pyrollidinone (NMP) solvent onto an Al foil substrate. The slurry was cast using a surgical blade. Cast laminates were first dried in air at 120 °C for 2 h and then in a vacuum at 70 °C for 8 h. Then they were pressed to a fixed thickness of 80−100 μm. Each electrode had the same weight of active matter (approximately 7.26 mg). Lithium coin cells (CR2032) were fabricated in an Ar filled glove box (<1 ppm O_2, MBraun, Germany), with lithium metal as the anode, Celgard 2400 microporous polypropylene membrane as the separator and electrolyte consisting of 1 M of $LiPF_6$ in a 1:1:1 volume fraction of ethylene carbonate (EC)/dimethyl carbonate/ethyl−methyl carbonate. Charge−discharge formation and GITT experiments were performed using a multichannel potentiostatic−galvanostatic system (CT2010A, Wuhan Land, China). For the GITT measurement, the coin cells were charged and discharged with a constant current flux for a given time, followed by an open-circuit rest for a specified time interval.

3. Results and discussion

Fig. 1 shows scanning electron micrographs (SEM) for the precursor (theoretical formula $Ni_{0.35}Mn_{0.65}(OH)_2$) and $0.3Li_2MnO_3 \cdot 0.7LiNi_{0.5}Mn_{0.5}O_2$ powders. It can be seen that the precursor particles have a uniform spherical morphology. Despite different calcination temperatures, the final $0.3Li_2MnO_3 \cdot 0.7LiNi_{0.5}Mn_{0.5}O_2$ particles retain a spherical shape after being re-crystallized with the lithium sources during the high temperature calcination process. In addition, the magnified images in Fig. 1 show that, as the calcination temperature increases, the primary particle of samples grows rapidly larger. Based on the approximate size-label, as shown in Fig. 1, and statistical calculations, the average size of the primary particle of samples are around 80 nm, 200 nm and 500 nm for LM-8, LM-9 and LM-10, respectively. Moreover, as the calcination temperature rose, the pores in the primary particles gradually disappeared and the spherical structure become more compact.

The particle distribution curves of the precursor and powders are shown in Fig. 2. Compared with the precursor, the D_{50} values of the three Li-rich materials were slightly reduced. This may be attributed to the grinding treatment after sintering. In addition, it can be seen that the three Li-rich materials have similar particle distribution curves and the median particle sizes D_{50} have almost the same value. This indicates that the sintering process hardly affected the secondary particle size. Moreover, compared with the precursor, the special surface areas of the final cathode materials decreased largely, as shown in the inset table in Fig. 2. During the high temperature calcination with lithium carbonate, the nano-primary particles fused to one another, resulting in larger primary particles without changing the morphology of the secondary particles. As the calcination temperature increased, with further crystal growth at the higher temperatures, the special surface area of the powders decreased from 4.959 to 0.676 m^2 g^{-1}. Subsequently, the clustering of the primary particles becomes tighter and tighter. These results are consistent with the SEM images. The compositions of the as-prepared composites are listed in Table 1. The elemental content corresponds to the formula given and has almost the same values for all three samples indicating that the chemical composition does not vary with calcination temperature.

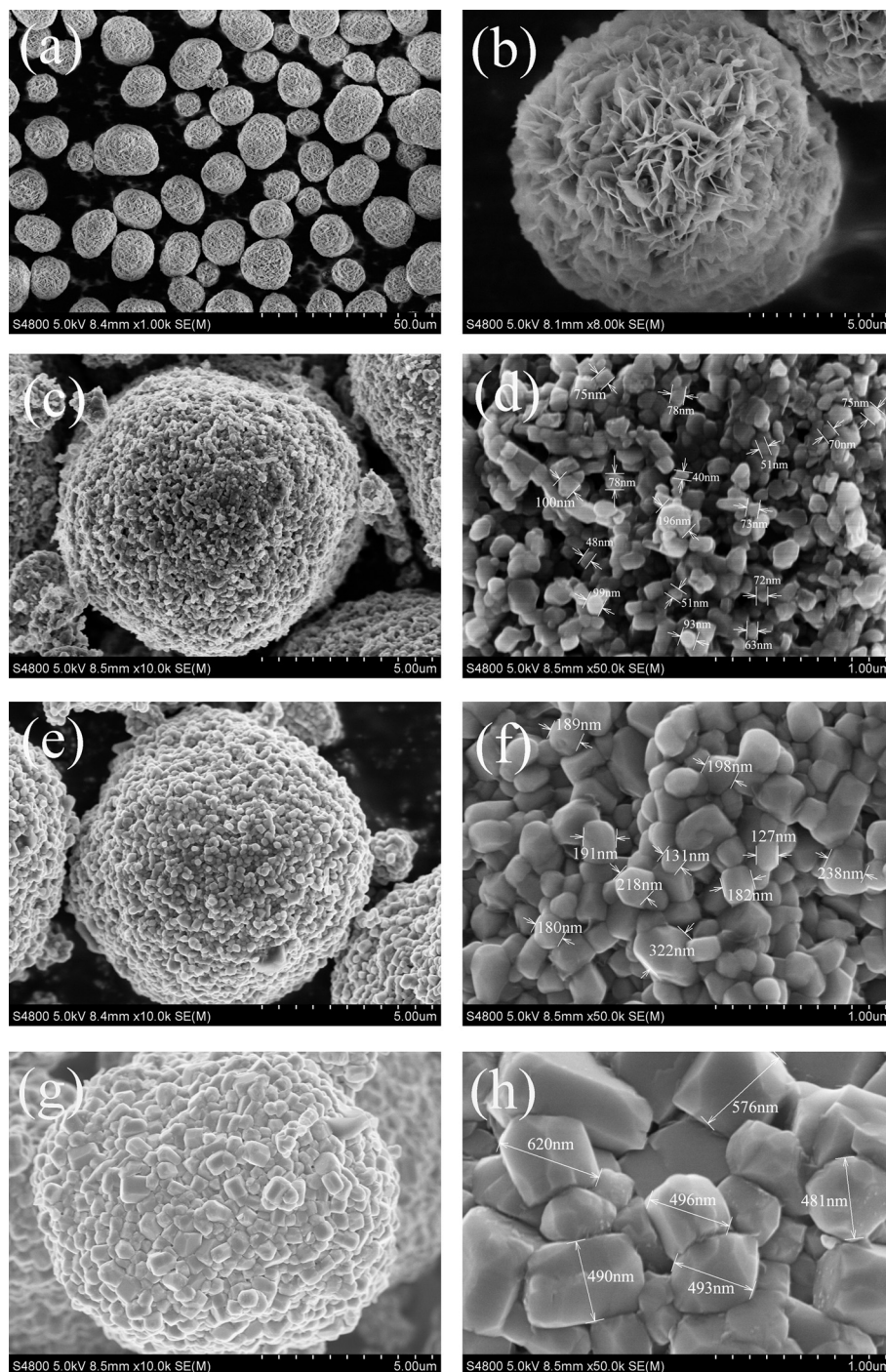XRD patterns of the $0.3Li_2MnO_3 \cdot 0.7LiNi_{0.5}Mn_{0.5}O_2$ powders are shown in Fig. 3. All the diffraction patterns can be indexed based on

Fig. 1. Scanning electron microscopy images: (a) and (b) are the precursor, with images of $0.3Li_2MnO_3 \cdot 0.7LiNi_{0.5}Mn_{0.5}O_2$ powders calcined at 800 °C (c), 900 °C (e), and 100 °C (g); (d), (f) and (h) are the magnified images of (c), (e) and (g), respectively.

a hexagonal α-NaFeO$_2$ structure with the *R-3m* space group. The peaks between 20° and 23°, highlighted by an arrow, can be identified as the (020) reflection of the super lattice structure of the Li$_2$MnO$_3$-like component (*C2/m* space group), as reported elsewhere [24–28]. Based on the *R-3m* structure, the lattice parameters and lattice strains of the samples can be calculated using Rietveld refinements; these are listed in Table 2. All samples exhibit *c/a* values greater than 4.9, which indicates an explicit crystalline layer structure [29]. The separations between the (108)/(110) peaks provide further evidence for a relatively ordered layer structure

[28]. The values of the lattice volumes show an increasing trend with calcination temperature and are consistent with earlier reports on layered cathode materials [30,31].

However, in the magnified XRD patterns (55°–75°) shown in Fig. 3, the widths of the diffraction peaks for the (108) and (110) crystal planes clearly increase from LM-10 to LM-8. In general, several factors can contribute to the broadening of diffraction peaks, including instrumental factors and sample factors. Of these factors, microstrain in the lattice is quite important [32,33]. In this work, the variation of residual strain in the lattice might be
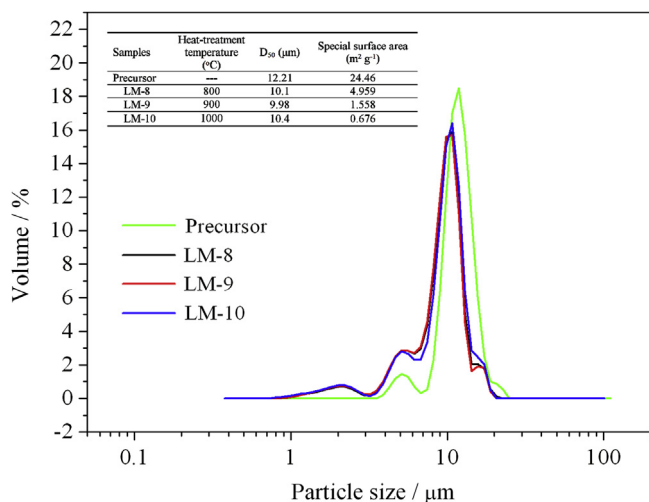
Fig. 2. The particle distribution curves of the $0.3Li_2MnO_3 \cdot 0.7LiNi_{0.5}Mn_{0.5}O_2$ powders.

Table 2
The crystal structure parameters and lattice strains of prepared powders, calculated by Rietveld refinements.

Samples	Primary particle size level (nm)	a (Å)	c (Å)	c/a	Volume (Å³)	Lattice strain%
LM-8	80	2.8606	14.2416	4.9784	100.92(9)	0.12779
LM-9	200	2.8605	14.2447	4.9797	100.94(6)	0.10869
LM-10	500	2.8606	14.2500	4.9814	100.98(8)	0.08059

of 25 mA g^{-1} between 2.5 and 4.8 V, are shown in Fig. 5(a). The initial charge process can be divided into two parts. The first one is the Li-extraction from the structure of space group *R-3m* accompanied by the oxidation of mainly Ni^{2+}/Ni^{4+} in the transition metal layer. The second charge process (above 4.5 V) corresponds to the activation of the Li_2MnO_3 component in the solid solution material [37—41]. The first columbic efficiencies for LM-8, LM-9 and LM-10 were 75.1% 72.6% and 61.18%, respectively (Fig. 5(a)). LM-8, LM-9 and LM-10 exhibited different initial discharge capacities. Different primary particle sizes may cause changes of Li$^+$ ion mobility and degree of polarization. A larger primary particle size might cause higher polarization and affect the Li$^+$ ion diffusion in the solid phase. It has been reported that by reducing the charge—discharge current rate or elevating the operating temperature, the polarization can be reduced and potential capacity of these Li-rich layered materials can be further enhanced [6]. In order to verify this point, we performed an additional test. In the secondary cycle, the same cells were used for a charge—discharge test at a rate of 0.05C at 55 °C; the resulting charge—discharge curves are shown in Fig. 5(b). Compared with capacities obtained in the first cycle (Fig. 5(a)), the capacities of all cells in the second cycle increased by a significant extent. This can be attributed to the activation effect produced by the high temperature and low charge—discharge current [6]. In addition, the three samples exhibit similar charge—discharge capacities, as expected. This confirms that the similar intrinsic

attributed to the different sintering temperatures. Higher lattice strain will hinder Li$^+$ migration during the electrochemical process and influence the structural stability of the active material in the charge/discharge cycle [34—36]. The lattice strains decrease as the primary particle size of the as-prepared cathode materials increases (Fig. 4 and Table 2). LM-8 has the smallest primary particle and the largest lattice strain. In contrast, the smallest lattice strain exists in LM-10, which is related to the high heat-treatment temperature. It implies that the layered structure becomes more established as the calcination temperature increases, enhancing Li$^+$ migration during the electrochemical reaction.

The initial charge—discharge voltage profiles of $Li/0.3Li_2MnO_3 \cdot 0.7LiNi_{0.5}Mn_{0.5}O_2$ coin cells, using a constant current density

Table 1
Chemical composition of the as-prepared cathode materials.

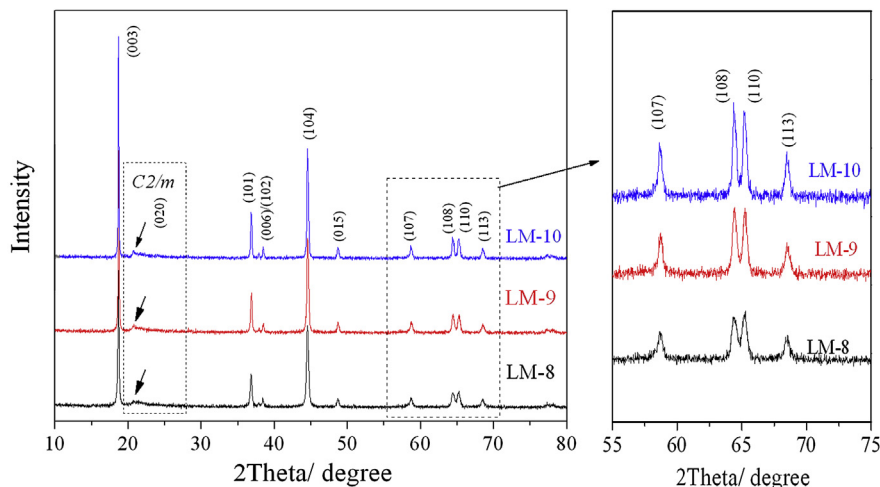| Samples	Theoretical composition	Element ratio in mole				Chemical formula
		Li	Ni	Mn	O	
LM-8	$Li_{1.130}Ni_{0.304}Mn_{0.565}O_2$	1.135	0.305	0.561	2.000	$Li_{1.135}Ni_{0.305}Mn_{0.561}O_2$
LM-9		1.129	0.304	0.562	2.000	$Li_{1.129}Ni_{0.304}Mn_{0.562}O_2$
LM-10		1.134	0.302	0.559	2.000	$Li_{1.134}Ni_{0.302}Mn_{0.559}O_2$

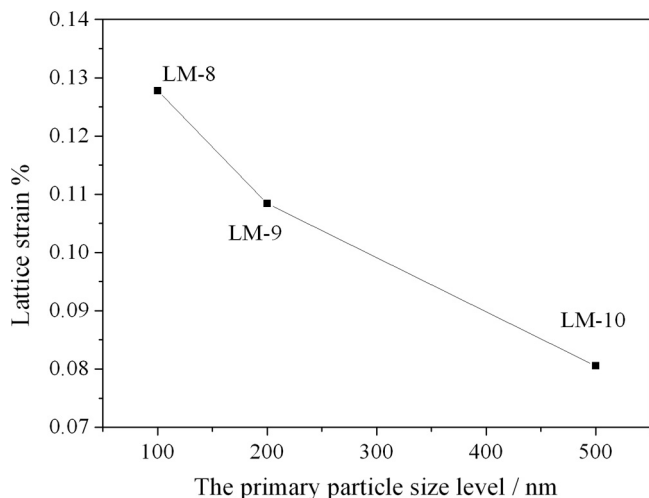**Fig. 3.** X-ray diffraction patterns of the as-prepared cathode materials.

Fig. 4. Lattice strain as a function of primary particle size.

Fig. 6. The discharge capacity as a function of discharge current density for Li/0.3Li$_2$MnO$_3$·0.7LiNi$_{0.5}$Mn$_{0.5}$O$_2$ coin cells. The test is performed at room temperature.

composition of these materials determines their similar intrinsic reversible capacity.

Fig. 6 shows the discharge capacity of the coin cells measured at different current densities at room temperature. Before the rate test, three cycles at a rate of 0.1C between 2.5 and 4.8 V were performed for each cell. It can be seen that, LM-8 has the highest
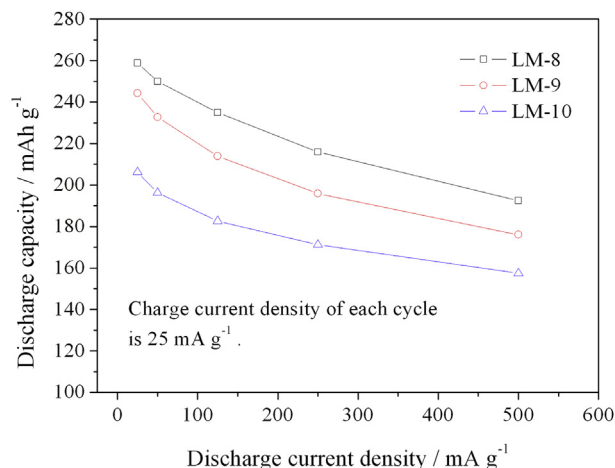
discharge capacity and LM-10 shows the lowest discharge capacity at all times. This result may be caused by the different electrochemical resistances of these materials resulting mainly from different primary particle sizes.

To further compare the kinetics of the lithium ion extraction and insertion of the prepared 0.3Li$_2$MnO$_3$·0.7LiNi$_{0.5}$Mn$_{0.5}$O$_2$ materials with different primary particle size, the chemical diffusion coefficient of the lithium ion (D_{Li^+}) in the active material is used. The chemical diffusion coefficient of a lithium ion is an important kinetic parameter for lithium-ion insertion and extraction reactions in intercalation materials. Based on chronopotentiometry at near-thermodynamic-equilibrium conditions, GITT is a reliable method to determine D_{Li^+}. Based on the GITT measurements, the chemical diffusion coefficient of Li$^+$ can be calculated using the following equation [42–47]:

$$D_{Li^+} = \frac{4}{\pi}\left(\frac{m_B V_M}{M_B S}\right)^2 \left(\frac{\Delta E_s}{\tau dE_x/d\sqrt{\tau}}\right)^2 \left(t << L^2/D_{Li^+}\right) \qquad (1)$$

where V_M is the molar volume of 0.3Li$_2$MnO$_3$·0.7LiNi$_{0.5}$Mn$_{0.5}$O$_2$, deduced from crystallographic data, M_B and m_B are the molecular weight and mass of the active material, respectively, and S is the active surface area of the electrode, deduced from BET testing.

If the E versus $\tau^{1/2}$ behavior is linear, then Eq. (1) can be simplified to the following [42,43,48]:

$$D_{Li^+} = \frac{4}{\pi}\left(\frac{m_B V_M}{M_B S}\right)^2 \left(\frac{\Delta E_s}{\Delta E_t}\right)^2 \qquad (2)$$

Usually, to obtain the steady state cell voltage, a small current flux and long time interval should be used for the GITT test. In this work, the GITT data were collected at a 0.05C rate ($\sim$12.5 mA g^{-1}) and a time interval of 240 min. Because the prepared Li-rich materials have similar chemical composition and lattice parameters, the molar volumes V_M of the three samples have almost the same values, 20.2585 cm^3 mol^{-1} for LM-8, 20.2625 cm^3 mol^{-1} for LM-9, and 20.2705 cm^3 mol^{-1} for LM-10. The active surface areas of the LM-8, LM-9 and LM-10 electrodes are 0.05505 m^2, 0.0346 m^2 and 0.01563 m^2, respectively. The differences in the active surface areas of the electrodes can be attributed to the different BET values of these powders. Before the GITT tests, three cycles at a rate of 0.1C between 2.5 and 4.8 V were performed at room temperature.

Fig. 7 shows the variation of the lithium ion diffusion coefficient (D_{Li^+}) as a function of the Li intercalation/de-intercalation content for the 0.3Li$_2$MnO$_3$·0.7LiNi$_{0.5}$Mn$_{0.5}$O$_2$/Li coin cells. Fig. 7(c) and (d)
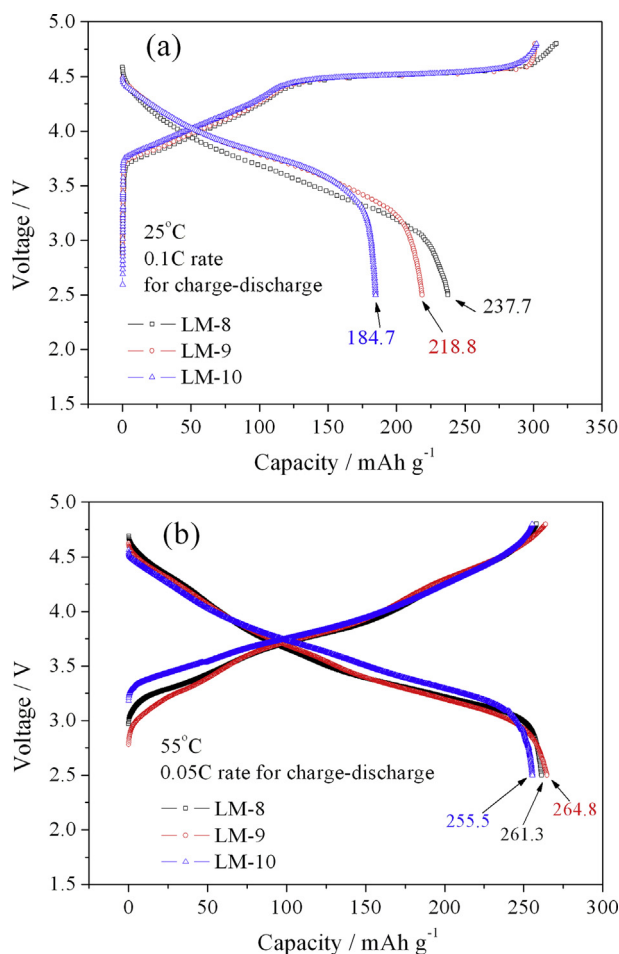

Fig. 5. The charge–discharge curves of Li/0.3Li$_2$MnO$_3$·0.7LiNi$_{0.5}$Mn$_{0.5}$O$_2$ coin cells (a) 25 °C, 0.1C for the initial cycle and (b) 55 °C, 0.05C for the second cycle; 250 mAh g^{-1} is used as the theoretical reversible capacity.

shows that the D_{Li^+} value of the three electrodes is about 10^{-13}–10^{-16} cm^2 s^{-1}, which agrees with earlier reports [28,45]. However, of the three samples, LM-8, with the smallest primary particle size, shows the lowest D_{Li^+} value; LM-10 with the largest primary particle size shows the biggest D_{Li^+} value, irrespective of charge or discharge. This may be attributed to the effect of the different crystallinity or lattice strain. A lattice with high lattice strain or low crystallinity would have more defects and result in a large resistance for Li migration in solid phase during the electrochemical reaction [32,49]. The data show that, for these three samples, the D_{Li^+} value increases as the primary particle size increases.

However, since LM-10/Li has the largest Li^+ diffusion capability, it is difficult to understand why LM-10/Li coin cells show relatively poor rate performance. According to the relationship $t \approx L^2/D_{Li^+}$, the Li^+ diffusion time t is determined by the diffusion length in the solid phase and the Li^+ diffusion parameter D_{Li^+}. Based on the hypothesis that the primary particle is spherical, half the primary particle diameter can be regarded as the Li^+ diffusion length in the solid phase during the electrochemical reaction. According to the SEM results (Fig. 1), the primary particle size L shows three distinct values, 80 nm for LM-8, 200 nm for LM-9 and 500 nm for LM-10. Therefore, calculating the distance from the center to the surface of a single primary particle, gives Li^+ diffusion lengths of 40 nm for LM-8, 100 nm for LM-9 and 250 nm for LM-10. If the primary particle size L_{LM-8} of LM-8 is set as L_0 and D_{Li^+} of LM-8 is set as D_0, the t_{LM-8} can be written as the following equation:

$$t_{LM-8} \approx L_0^2/D_0 \tag{3}$$

Thus, according to the primary particle size relationship, L_{LM-9} and L_{LM-10} can be expressed using $2.5L_0$ and $6.25L_0$. Here, we make the calculation using an OCV of about 4.0 V, as an example. According to Fig. 7(c), at an OCV of about 4.0 V, the D_{Li^+} of LM-8, LM-9 and LM-10 are 1.27E-15, 3.42E-15 and 1.79E-14 cm^2 s^{-1}, respectively. The value D_{Li^+} of LM-10 is about 14 times greater than that of
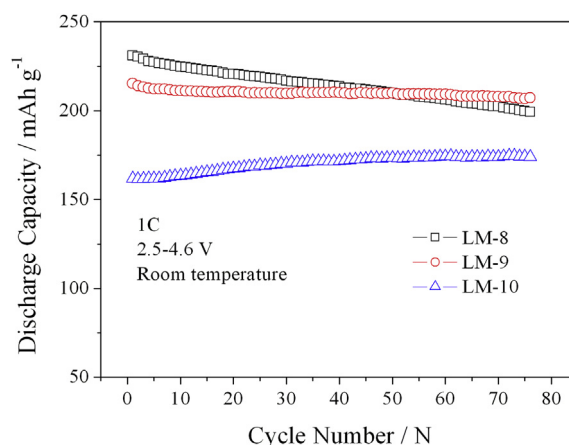

Fig. 8. The cyclic curves of $Li/0.3Li_2MnO_3 \cdot 0.7LiNi_{0.5}Mn_{0.5}O_2$ coin cells. The charge–discharge rate is 1C (250 mA g^{-1}).

LM-8. The primary particle size L_{LM-10} is about 6.25 times that of L_{LM-8}. So, the Li^+ diffusion time t in solid phase of LM-10 can be calculated as follows:

$$t_{LM-10} \approx L_{LM-10}/D_{Li^+(LM-10)} = (6.25L_0)^2/(14\,D_0)$$
$$= 2.8L_0^2/D_0 \approx 2.8t_{LM-8}$$

Therefore, even though it has the largest D_{Li^+} parameter, the Li^+ diffusion time t in solid phase of LM-10 is about 2.8 times of that of LM-8. Similar calculations can be carried out for LM-9, revealing that the Li^+ diffusion time t of LM-9 in the solid phase is about 2.3 times that of LM-8. This analysis verifies that the effect of the diffusion length on the electrochemical kinetics is greater than the Li^+ diffusion parameter D_{Li^+}, supporting other reports [19,49].
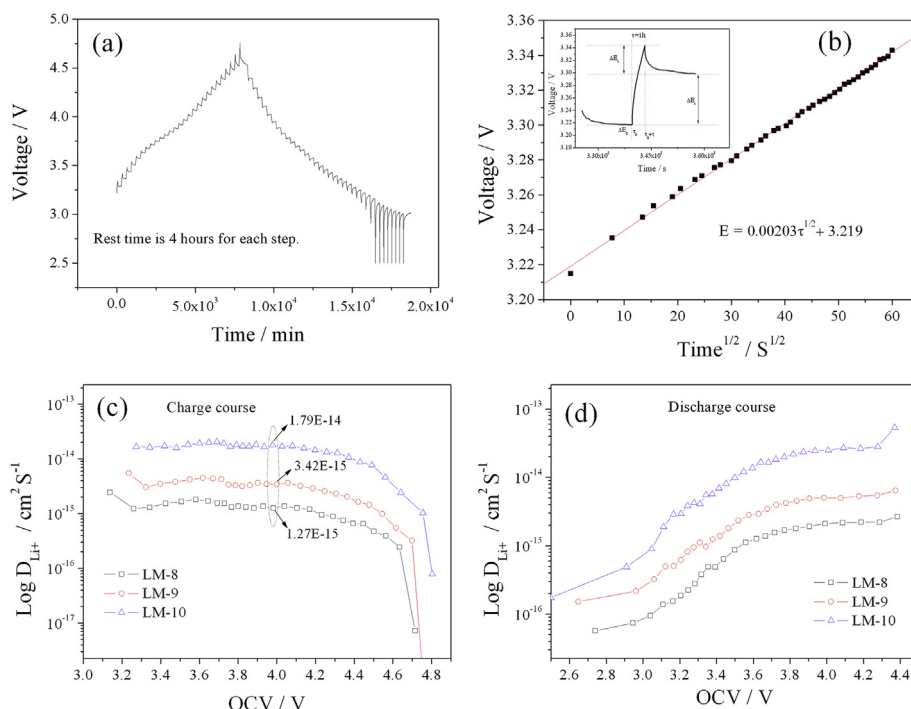

Fig. 7. Li-ion diffusion coefficient for samples obtained by GITT. (a) GITT curve of LM-8. (b) Relationship of the LM-8/Li cell voltage as a function of $\tau^{1/2}$ for one titration; inner figure is τ vs. E profile of a LM-8/Li coin cell for a single GITT titration. (c) $\log(D_{Li})$ as a function of the OCV in the charge process. (d) $\log(D_{Li})$ as a function of the OCV in the discharge process.

Fig. 8 shows the cyclic curves of Li/0.3Li$_2$MnO$_3$·0.7LiNi$_{0.5}$Mn$_{0.5}$O$_2$ coin cells, obtained at 25 °C with a constant current density of 250 mA g^{-1} between 2.5 and 4.6 V. Before each cyclic test, three cycles between 2.5 and 4.8 V with a 0.1C charge–discharge rate were performed for each cell. The LM-8 sample exhibits the highest capacity in the initial stage, but the largest tendency for capacity decay. LM-10 has relatively low capacity in the initial stage. As the cycle number increases, the discharge capacity of LM-10 shows an increasing trend. The relatively low initial discharge capacity can be attributed to that fact that the activation of Li$_2$MnO$_3$ cannot be completed during the initial stage of the cycle due to the large primary particle size. During the subsequent cycling process, the Li$_2$O extraction from Li$_2$MnO$_3$ can be completed gradually during the cycling, resulting in an increase in capacity. This phenomenon agrees with earlier reports [41,50,51]. It is well known that the cyclic performance of a material is an integrative parameter, affected by crystallite size, particle morphology and crystallinity. Small crystal strain implies good crystallinity, which is an essential condition to obtain good electrochemical performance and to maintain structural stability during cycling [35]. Compared with LM-8 and LM-10, LM-9 exhibits the best integrated cyclic performance, with relatively high initial discharge capacity and stable cycling. This may be attributed to having optimum primary particle size, special surface area and small lattice strain.

4. Conclusions

In this paper, we describe the successful synthesis of a series of 0.3Li$_2$MnO$_3$·0.7LiNi$_{0.5}$Mn$_{0.5}$O$_2$ materials, which have different primary particle sizes, but similar secondary particle sizes. SEM results indicate that, with increasing calcination temperature, the sizes of the powder primary particles increase and the special surface areas decrease. However, they have similar particle size distributions. XRD analysis shows that these are typical Li-rich layered materials with characteristic Li$_2$MnO$_3$ diffraction peaks. ICP results show that they are of similar chemical composition. As the primary particle size increases, the rate discharge performance of the materials decreases. However, the GITT results show that the sample LM-10, with the largest average particle size of 500 nm, has the largest Li$^+$ ion diffusion capability in the solid phase; LM-8 with the smallest average particle size of 80 nm, has the smallest Li$^+$ ion diffusion capability. Combined with a rate test, this verifies that it is more effective to raise the rate performance by shortening the diffusion lengths rather than raising the chemical diffusion coefficient of Li$^+$ ions in the solid phase. In this work, the LM-9 material shows the best integrated electrochemical performance, due to having optimum primary particle size, BET and relatively low lattice strain.

Acknowledgments

References

[1] M.M. Thackeray, S.H. Kang, C.S. Johnson, J.T. Vaughey, R. Benedek, S.A. Hackney, J. Mater. Chem. 17 (2007) 3112.
[2] D.Y.W. Yu, K. Yanagida, H. Nakamura, J. Electrochem. Soc. 157 (2010) A1177.
[3] J. Liu, A. Manthiram, J. Mater. Chem. 20 (2010) 3961.
[4] S.H. Kang, M.M. Thackeray, Electrochem. Commun. 11 (2009) 748.
[5] B. Song, M.O. Lai, L. Lu, Electrochim. Acta 80 (2012) 187.
[6] C.S. Johnson, N. Li, C. Lefief, M.M. Thackeray, Electrochem. Commun. 9 (2007) 787.
[7] F. Lian, M. Gao, W.H. Qiu, P. Axmann, M.M. Wohlfahrt, J. Appl. Electrochem. 42 (2012) 409.
[8] S.H. Kang, K. Amine, J. Power Sources 119 (2003) 150.
[9] C.W. Park, I.R. Mangani, H.W. Ryu, C.J. Park, J.S. Lee, S.J. Song, J.H. Moon, J. Kim, J. Phys. Chem. Solids 68 (2007) 1126.
[10] C.S. Johnson, N. Li, C. Lefief, J.T. Vaughey, M.M. Thackeray, Chem. Mater. 20 (2008) 6095.
[11] J. Liu, B.R. Jayan, A. Manthiram, J. Phys. Chem. C 114 (2010) 9528.
[12] J.M. Zheng, Z.R. Zhang, X.B. Wu, Z.X. Dong, Z. Zhu, Y. Yang, J. Electrochem. Soc. 155 (2008) A775.
[13] B. Liu, Q. Zhang, S.C. He, Y.C. Sato, J.W. Zheng, D.C. Li, Electrochim. Acta 56 (2011) 6748.
[14] Y. Wu, A. Manthiram, Solid State Ionics 180 (2009) 50.
[15] P.G. Bruce, B. Scrosati, J.M. Tarascon, Angew. Chem. Int. Ed. 47 (2008) 2930.
[16] A.S. Arico, P. Bruce, B. Scrosati, J.M. Tarascon, W.V. Schalkwijk, Nat. Mater. 4 (2005) 366.
[17] H. Zhang, X. Yu, P.V. Braun, Nat. Nanotechnol. 6 (2011) 277.
[18] M.S. Park, Y.M. Kang, G.X. Wang, S.X. Dou, H.K. Liu, Adv. Funct. Mater. 18 (2008) 455.
[19] Y.L. Ding, X.B. Zhao, G.S. Cao, T.J. Zhu, H.M. Yu, C.Y. Sun, J. Mater. Chem. 21 (2011) 9475.
[20] M. Kunduraci, J.F. Al-Sharab, G.G. Amatucci, Chem. Mater. 18 (2006) 3585.
[21] E. Hosono, T. Kudo, I. Honma, H. Matsuda, H.S. Zhou, Nano Lett. 9 (2009) 1045.
[22] S.B. Park, H.C. Shin, W.G. Lee, W.I. Cho, H. Jang, J. Power Sources 180 (2008) 597.
[23] Z. Lu, J.R. Dahn, J. Electrochem. Soc. 149 (2002) A815.
[24] M.M. Thackeray, C.S. Johnson, J.T. Vaughey, J. Mater. Chem. 15 (2005) 2257.
[25] A.D. Robertson, P.G. Bruce, Chem. Mater. 15 (2003) 1984.
[26] S.H. Kang, S.H. Park, C.S. Johnson, K. Amine, J. Electrochem. Soc. 154 (2007) A268.
[27] I. Belharouak, G.M. Koenig, J.J. Ma, D.P. Wang, K. Amine, Electrochem. Commun. 13 (2011) 232.
[28] J. Lin, D.B. Mu, Y. Jin, B.R. Wu, Y. Ma, F. Wu, J. Power Sources 230 (2013) 76.
[29] K.M. Shaju, G.V. Subba Rao, B.V.R. Chowdari, Electrochim. Acta 48 (2002) 145.
[30] B.J. Hwang, Y.W. Tsai, C.H. Chen, R. Santhanam, J. Mater. Chem. 13 (2003) 1962.
[31] D.K. Lee, S.H. Park, K. Amine, H.J. Bang, J. Parakash, Y.K. Sun, J. Power Sources 162 (2006) 1346.
[32] Y. Shin, A. Manthiram, Electrochem. Solid-State Lett. 5 (2002) A55.
[33] N. Amdouni, H. Zarrouk, F. Soulette, C. Julien, Mater. Chem. Phys. 80 (2003) 205.
[34] S. Dargaville, T.W. Farrell, Electrochim. Acta 94 (2013) 143.
[35] M.M. Thackeray, J. Electrochem. Soc. 142 (1995) 2558.
[36] D. Tong, J.L. Cao, Q.Y. Lai, A.D. Tang, Mater. Chem. Phys. 100 (2006) 217.
[37] Y. Wu, A. Manthiram, J. Power Sources 183 (2008) 749.
[38] L.Y. Yu, W.H. Qiu, J.Y. Huang, F. Lian, Mater 16 (2009) 458.
[39] G.Y. Kim, S.B. Yi, Y.J. Park, H.G. Kim, Mater. Res. Bull. 43 (2008) 3543.
[40] C.S. Johnson, J.S. Kim, C. Lefief, N. Li, J.T. Vaughey, M.M. Thackeray, Electrochem. Commun. 6 (2004) 1085.
[41] J.H. Lim, H. Bang, K.S. Lee, K. Amine, Y.K. Sun, J. Power Sources 189 (2009) 571.
[42] K.M. Shaju, G.V.S. Rao, B.V.R. Chowdari, Electrochim. Acta 49 (2004) 1565.
[43] X.H. Rui, N. Ding, J. Liu, C. Li, C.H. Chen, Electrochim. Acta 55 (2010) 2384.
[44] Z. Li, F. Du, X. Bie, D. Zhang, Y. Cai, X. Cui, C. Wang, G. Chen, Y. Wei, J. Phys. Chem. C 114 (2010) 22751.
[45] H. Yu, Y. Wang, D. Asakura, E. Hosono, T. Zhang, H. Zhou, RSC Adv. 2 (2012) 8797.
[46] K.M. Shaju, R.G.V. Subba, B.V.R. Chowdari, Electrochim. Acta 48 (2003) 2691.
[47] E. Deiss, Electrochim. Acta 50 (2005) 2927.
[48] J.H. Liu, X.M. Sun, Y.N. Li, X.Q. Wang, Y. Gao, K. Wu, N.N. Wu, B.R. Wu, J. Power Sources 245 (2014) 371.
[49] M. Gu, I. Belharouak, J. Zheng, H. Wu, J. Xiao, A. Genc, K. Amine, S. Thevuthasan, D.R. Baer, J.G. Zhang, N.D. Browning, J. Liu, C. Wang, ACS Nano 7 (2013) 760.
[50] S.J. Jin, K.S. Park, M.H. Cho, C.H. Song, A.M. Stephan, K.S. Nahm, Solid State Ionics 177 (2006) 105.
[51] S.H. Park, Y. Sato, J.K. Kim, Y.S. Lee, Mater. Chem. Phys. 102 (2007) 225.